Impact of a resonant magnetic perturbation field on impurity radiation, divertor footprint, and core plasma transport in attached and detached plasmas in the Large Helical Device

Impact of resonant magnetic perturbation field on impurity radiation, divertor footprint, and core plasma transport in attached and detached plasmas in LHD

M. Kobayashi[1,2], R. Seki[1,2], S. Masuzaki[1,2], S. Morita[1,2], H.M. Zhang[2], Y. Narushima[1,2], H. Tanaka[3], K. Tanaka[1,2], T. Tokuzawa[1,2], M. Yokoyama[1,2], T. Ido[1,2], I. Yamada[1,2], and the LHD Experimental Group[1]

[1] National Institute for Fusion Science, National Institutes of Natural Sciences, Toki, Japan
[2] SOKENDAI, Department of Fusion Science, Toki, Japan
[3] Graduate School of Engineering, Nagoya University, Chikusa-ku, Nagoya 464-8603, Japan

E-mail: kobayashi.masahiro@nifs.ac.jp

Received xxxxxx
Accepted for publication xxxxxx
Published xxxxxx

Abstract

Effects of resonant magnetic perturbation (RMP) field on impurity radiation, divertor footprint distribution, and core plasma transport are investigated in the detachment discharges of LHD. The RMP with m/n = 1/1 mode creates edge magnetic island in the stochastic layer, which enhances the impurity emission from low charge states, C^{2+} and C^{3+}, and then triggers detachment transition. The emission from the higher charge states, C^{4+} and C^{5+}, implies enhanced penetration of impurity during detachment phase with RMP. The toroidal divertor particle flux distribution exhibits n = 1 mode structure in both attached and detached phases, but with a large toroidal phase shift between the two phases. The distribution in the attached phase is well correlated with magnetic footprint of field line connection length calculated by the vacuum approximation. During the detached phase, however, the phase shift is not well explained by the vacuum approximation, where significant plasma response to the external RMP is observed. The energy confinement time becomes systematically shorter with RMP application due to the shrinkage of plasma volume caused by the edge magnetic island. On the other hand, the pressure profile during detachment with RMP is found to be more peaked than without RMP. The analysis with the core transport code TASK3D, taking into account heating profiles of NBI, shows no significant transport degradation during detachment with RMP application, whilst the enhanced radiation, the reduced divertor flux, and the possible impurity penetration.

Keywords: Detachment, Resonant magnetic perturbation field, Divertor, Impurity emission, Core plasma transport

1. Introduction

Divertor power handling is one of the most important issues for a nuclear fusion reactor. Divertor detachment operation is the most promising scheme for this purpose, where enhanced

edge radiation from impurity dissipates the plasma energy flux over a wide area of plasma facing components. It is, however, not yet clear whether the divertor power load is mitigated below the engineering limit with the detachment operation while maintaning the good core plasma confinement. It is often observed that during detached phase with high radiation fraction the core confinement degrades [1,2]. The cause for the degradation is considered due to enhanced interaction of plasma with recycling neutrals, or to impurity penetration into the confinement region, or enhancement of turbulence transport. The mechanism of the degradation has not been fully understood.

On the other hand, resonant magnetic perturbation (RMP) field has been found to be an effective tool to mitigate or suppress the edge localized mode (ELM) in tokamaks [3,4,5], and also to control edge plasma transport [6,7]. While the RMP is planned to be used in ITER, too [8,9,10], it is not yet clear how the RMP application affects the core plasma performance and the detachment operation. Change of the divertor power load distribution caused by the RMP application has also been pointed out, where at some places the power load even increases due to the 3D deformation of the magnetic field flux tubes connecting to the divertor plates [10,11]. Currently, these issues are under investigation as the highest priority [12,13,14].

In LHD (Large Helical Device), it has been found that the RMP application provides enhanced edge radiation and easy access to stable detachment operation [15]. The edge magnetic island induced by the RMP is considered to be responsible for the radiation enhancement, although the mechanism of the stabilization of the detachment is not yet clear. The EMC3-EIRENE simulations show enhanced radiation around the X-point of the edge island [15]. Space resolved measurements of radiation and impurity line emissions are in qualitative agreement with the simulation results [16,17], indicating selective cooling around the edge island region. Change of the recycling pattern at the plasma facing component during the detached phase with RMP has also been pointed out [18], which is considered due to the change of 3D edge magnetic field structue. Finally, the core plasma confinement characteristics during the detached phase with RMP is also an important issue, as mentioned above, which has been addressed in the previous study [19], but still requires more detailed analysis.

In this paper, we investigate the 3D structure of the divertor detachment distribution, which is found to be not uniform in toroidal direction with RMP application, which is correlated with connection length distribution at the divertor plates to a certain extent. Change of radiated power loss caused by the RMP in relation to the contribution from the different charge states impurity ions is discussed. The core plasma characteristics, such as plasma parameter profiles, energy confinement time, transport coefficient etc., during

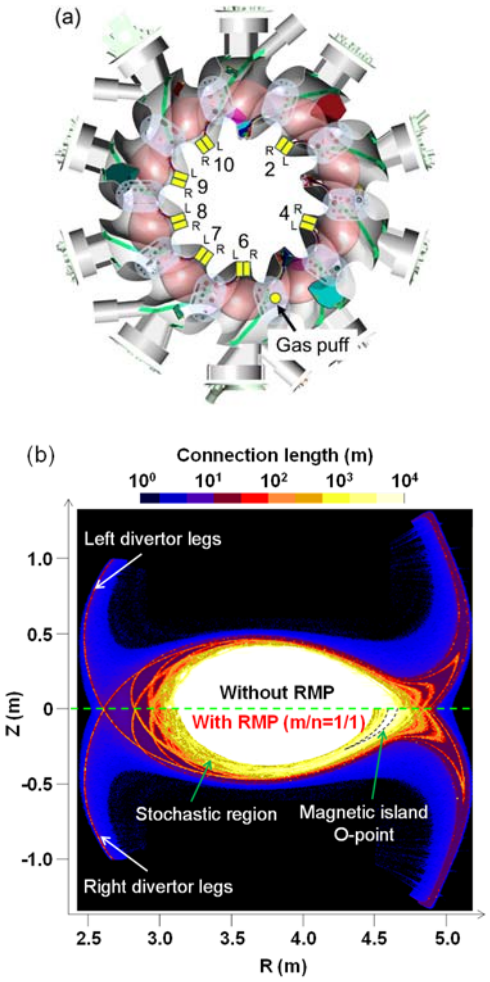

Fig.1 (a) Top view of the LHD torus. The location of the divertor probe arrays at the inboard side is indicated with toroidal section numbers. The letters "L" and "R" represent the "Left" and "Right" divertor arrays, which are connected to the left and right divertor legs, respectively, shown in (b). (b) Magnetic field line connection length (L_C) distribution on the poloidal cross section (toroidal section #6). The upper and lower halves show L_C without and with RMP application, respectively. The O-point of the remnant magnetic island is located at the outboard side on this cross section.

detachment phase with and without RMP application are investigated by using a core transport code. The paper is organized as follows. In Section 2, the edge magnetic field structure of LHD and typical detachment discharge with RMP are presented together with the measurements of radiated power and impurity emissions and with the divertor particle flux distributions as a measure of the detachment. In Section 3, the core plasma characteristics are analyzed using core transport code. The paper is summarized in Section 4.

2. Divertor detachment discharge with RMP

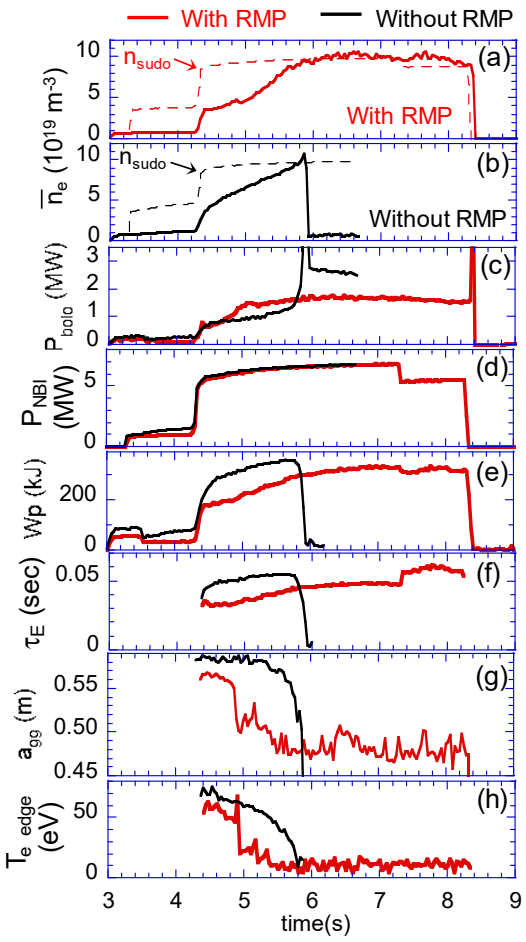

Fig.2 Time traces of (a, b) line averaged density, (c) radiated power measured by bolometer, (d) NBI heating power, (e) plasma stored energy, (f) energy confinement time, (g) radius of plasma volume, a_{99}, and (h) T_e at the edge region (averaged over R = 3.0 - 3.1 m) measured by Thomson scattering. The black and red lines represent the cases without (#128195) and with (#128188) RMP application. a_{99} is defined as a radius of plasma volume that contains 99% of total stored energy. The dashed lines in (a,b) represent the Sudo density limit.

2.1 Edge magnetic field structure in LHD

LHD is a heliotron type helical device with a poloidal winding number l = 2 and toroidal field period of n = 10 [20,21]. Because of the periodicity of the magnetic field structure, the LHD torus is divided into 10 toroidal sections, as shown in the top view of the torus of Fig.1 (a). Major radius and averaged minor radius are 3.9 m and ~ 0.54 m, respectively. The divertor plates are made of graphite and the first wall is covered by stainless steel tiles. The RMP is applied by the perturbation coils installed at top and bottom of the torus, which produce m/n=1/1 mode perturbation. Figure 1 (b) shows a poloidal cross section of the magnetic field connection length (L_C) distribution of LHD, where upper and lower halves show the L_C without and with RMP application, respectively. In the edge region of LHD there exists inherently stochastic magnetic field structure, which is induced by the mode spectrum of magnetic field of the helical coils. LHD has an iota (inverse of safety factor) profile which increases from ~ 0.5 at the center of plasma to > 1 toward the edge region. Thus the RMP resonates at the periphery of the plasma. In order to place the resonant layer at the edge stochastic layer, we select a magnetic configuration with a magnetic axis (R_{ax}) at R = 3.9 m and B_t = 2.54 T (clockwise direction in the top view of torus). In this configuration, the m/n=1/1 magnetic island is created in the edge stochastic layer, as shown in the lower half of Fig.1 (b). The O-point of the remnant magnetic island is visible, which is located at the outboard side of toroidal section #6. The maximum perturbation strength is $\tilde{B}_r/B_0$~ 0.1 %, which was applied for the discharges analyzed in this paper. The m/n = 1/1 island rotates in poloidal direction (θ) with changing toroidal angle (ϕ) according to iota $= \frac{d\theta}{d\phi} =$ 1 magnetic field line. When they come close to the helical coils, the island width becomes narrow due to the increased B field strength.

2.2 Discharges with and without RMP

Figure 2 shows time traces of plasma parameters in the density ramp-up discharges with (red lines) and without (black lines) RMP application without auxiliary impurity seeding. The time traces are shown for t ≥3.0 sec, where the NB (neutral beam) heating started at t = 3.3 sec following plasma initiation by the electron cyclotron heating. The RMP field is applied before the heating starts. The same input power of NB and gas puff sequences are applied for the both cases (Fig.2 (d)). Shown by dashed curves in Fig.2 (a) and (b) are the density limit derived by a semi empirical scaling based on the radiation power balance in helical devices, which is defined as, $n_{Sudo} = 0.25(PB/a^2/R)^{0.5}\ (10^{20}m^{-3})$ [22]. Here $P, B, a, and\ R$ are heating power (MW), magnetic field (T), minor radius (m) and major radius (m), respectively. $B, a, and\ R$ are fixed to 2.54 T, 0.536 m, and 3.90 m for the both cases with and without RMP in the present analysis. Without RMP, the density ramp-up leads to sudden increase in radiated power as approaching the density limit, as shown in Fig.2 (c), P_{bolo}, which is measured by a resistive bolometer at toroidal section #3. The main radiator is carbon originating from the divertor plates. It still remains under discussion whether P_{bolo} represents total radiated power in the whole torus or not, because of the difficulties in the measurement of 3D radiation structure in the helical devices. Once such sudden increase of radiation is encountered, it is difficult to tame the evolution and the discharge results in radiation collapse at t = 5.9 sec.

With RMP application, the density ramp-up also leads to increase in the radiation as observed around t = 4.9 sec, but it is stabilized at elevated level without collapse. The discharge is sustained around the density limit until the end of NBI

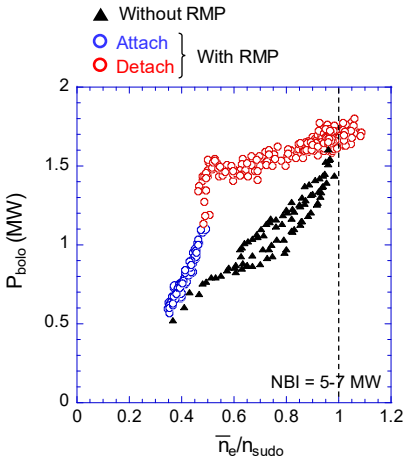

Fig.3 Radiated power measured by bolometer as a function of the line averaged density normalized by the Sudo density limit. Black triangles: without RMP. Blue circles: attached phase with RMP. Red circles: detached phase with RMP. The data of NBI heating of 5 to 7 MW are plotted.

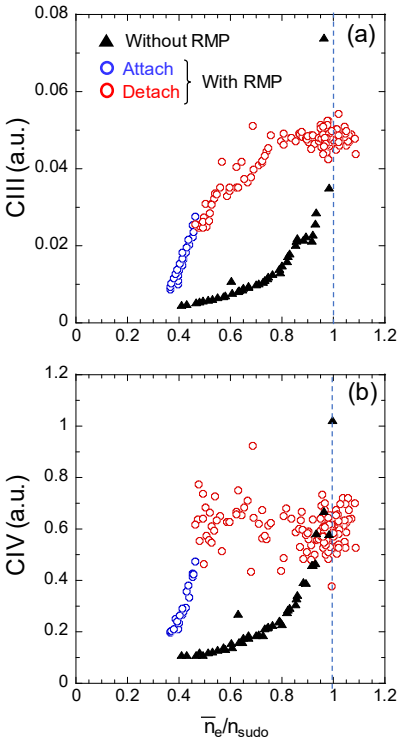

Fig.4 The density dependence of (a) CIII (97.7 nm, 2s2p-$2s^2$) and (b) CIV (154.8 nm, 2p-2s) measured by spectrometer at toroidal section #10. Black triangles: without RMP. Blue circles: attached phase with RMP. Red circles: detached phase with RMP.

heating as shown in Fig.2 (a). Figure 2 (g) plots the plasma radius, a_{99}, which is defined as a radius of volume that contains 99% of total stored energy. a_{99} is calculated based on the

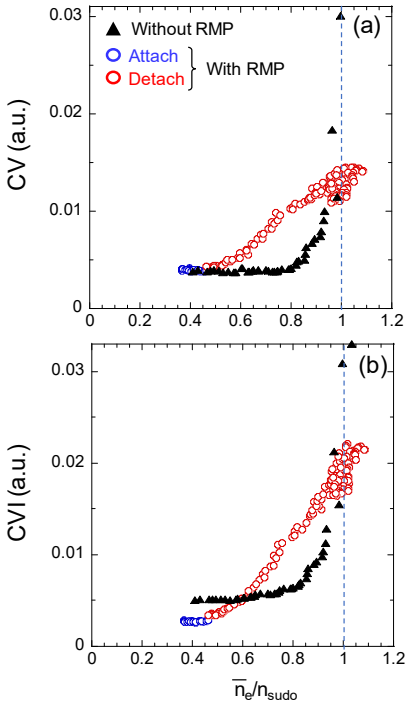

Fig.5 The density dependence of (a) CV (4.0 nm, 1s2p-$1s^2$) and (b) CVI (3.4 nm, 2p-1s) measured by spectrometer at toroidal section #10. Black triangles: without RMP. Blue circles: attached phase with RMP. Red circles: detached phase with RMP.

equilibrium mapping technique developed in LHD data acquisition system [23]. a_{99} is clearly smaller in the case with RMP than without RMP. This is due to the edge magnetic island, which extends the stochastic layer radially inward [19]. a_{99} decreases sharply at t = 4.9 sec, which corresponds to the timing of increase in radiated power. It is also shown that the edge T_e, which is measured by Thomson scattering (averaged over R = 3.0 – 3.1 m), decreases at the same timing as shown in Fig.2 (h). In the present analysis, we define the detachment transition at t = 4.9 sec, where the strong shrinkage of plasma volume as well as edge cooling takes place due to the strong edge radiation. As shown below, the behaviour of divertor particle flux is not straightforward to determine the timing of detachment transition. The plasma stored energy, W_p, and the energy confinement time, τ_E, are systematically smaller with RMP application due to the smaller plasma volume, both of which, however continue to increase after the detachment transition.

In the following sections, we analyse the well diagnosed selected discharges from the 18th cycle experiments in LHD.

2.3 Effects of RMP on impurity radiation

The significant different behaviour between the cases with and without RMP is observed in the density dependence of radiated power (P_{bolo}), which is plotted in Fig. 3. Without

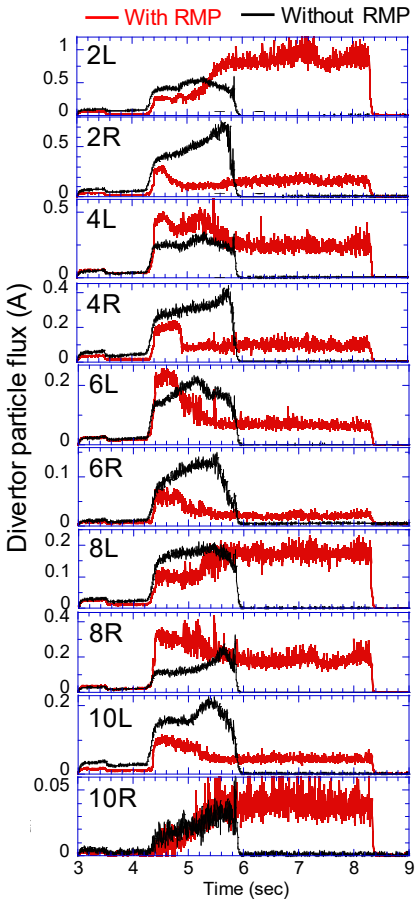

Fig.6 The time traces of divertor particle flux at different toroidal sections, #2, 4, 6, 8, 10. The letter "L" and "R" represent "Left" and "Right" divertor plate array (Fig.1). Black: without RMP. Red: with RMP.

RMP, the radiated power shows rapid increase around the density limit, $\bar{n}_e/n_{Sudo} \sim 1$, i.e. $\left.\frac{\partial P_{bolo}}{\partial n_e}\right|_{without\ RMP} \sim \infty$. This indicates that any small density perturbation leads to significant change in radiation, and thus the system is unstable. On the other hand, with RMP, the radiation is enhanced at lower density, $\bar{n}_e/n_{Sudo} \sim 0.4$, and then transits to the detached phase. After the detachment transition, the density dependence of radiated power becomes much weaker, $\left.\frac{\partial P_{bolo}}{\partial n_e}\right|_{with\ RMP} \ll \left.\frac{\partial P_{bolo}}{\partial n_e}\right|_{without\ RMP}$. This provides easier control of the radiation level with density, which is one of the control knobs by gas puff. It is also noted that, with the suppressed $\left.\frac{\partial P_{bolo}}{\partial n_e}\right|_{with\ RMP}$, the discharge can be sustained stably around the density limit, $\bar{n}_e/n_{Sudo} = 1$. The increase of radiation at the lower density with RMP is interpreted due to the increased low T_e volume, 10~20 eV, caused by edge magnetic island, which is favoured by lower charge state emission of carbon as analysed in ref [15,19].

The carbon resonance line emissions are measured by VUV and EUV spectrometers in LHD [24]. Figure 4 shows density dependence of CIII and CIV emissions as a function of density. These emissions of the low charge states have been identified as dominating radiation power loss during detachment [24]. The significant increase of CIV and CIII at the low density ($\bar{n}_e/n_{Sudo} \sim 0.4$) with RMP is observed, which probably triggers the detachment transition. After the transition, CIV saturates while CIII continues to increase up to $\bar{n}_e/n_{Sudo} \sim 0.8$, and then saturates around the density limit. The behaviour is qualitatively consistent with the density dependence of P_{bolo}.

The contribution of CV and CVI emissions to the total radiative power loss was found to be small [24]. Here we plot the higher charge state emission, CV and CVI in Fig.5. Since the ionization potential of CV and CVI are 392 and 490 eV, respectively, these quantities can be a proxy for impurity contents inside/around LCFS. Without RMP, both CV and CVI stay nearly constant with increasing density up to $\bar{n}_e/n_{Sudo} \sim 0.8$. At $\bar{n}_e/n_{Sudo} > 0.8$, both of them increase rapidly indicating impurity penetration into confinement region, leading to radiative collapse. With RMP application, CV and CVI also stay nearly constant with increasing density but only at the attached phase, $\bar{n}_e/n_{Sudo} < 0.45$. At this lower density range, CVI is substantially smaller than that without RMP. This could be due to better impurity screening with edge magnetic island [25,26]. After the detachment transition, both emissions start to increase toward higher density range, where CV changes its slope at $\bar{n}_e/n_{Sudo} \sim 0.8$, while CVI continues to increase with the same rate. The rapid increase of the emissions as observed in the case without RMP is, however, avoided even around the density limit, $\bar{n}_e/n_{Sudo} \sim 1.0$.

These results show clear change of edge impurity radiation process and impurity transport between the cases with and without RMP, which provides a key role in the detachment stabilization. The measurements of impurity emissions and radiated power distributions have shown the enhancement of radiative loss around the magnetic island, which is in qualitative agreement with EMC3-EIRENE simulation [15,16]. The mechanism of the stabilization of the radiation layer is under investigation taking into account the geometry of the magnetic island as well as the energy transport parallel and perpendicular to the magnetic field lines. Similar phenomena on the detachment stabilization with large island was also found in W7-AS [27]. The recent results of the successful detachment control from W7-X with the island divertor also suggest an important role of the edge magnetic island on detachment stabilization [28]. Impurity profile analysis in the confinement region, which might affect core energy transport as discussed later in the next section, is also left for future work.

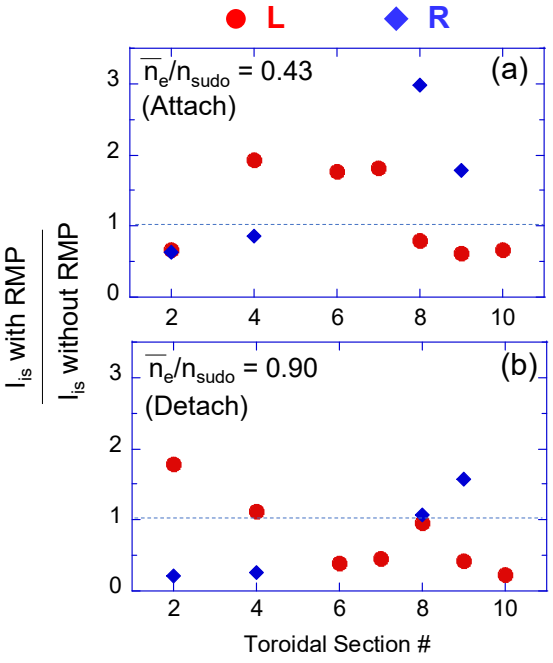

Fig.7 Toroidal distributions of divertor particle flux with RMP (summed over 20 probe pins at each section) normalized by those without RMP. (a) $\bar{n}_e/n_{Sudo}$ = 0.43 (attached with RMP), (b) $\bar{n}_e/n_{Sudo}$ = 0.90 (detached with RMP). Red circles: "L," Left divertor, blue diamonds: "R," right divertor arrays. The sections with malfunction of probe pins around strike line are excluded.

2.4 Effects of RMP on toroidal asymmetry of detachment

Because of the n = 1 mode structure in the RMP, a toroidal asymmetry is induced for the divertor particle flux distribution, which can lead to toroidal asymmetry of detachment. The divertor particle flux distributions are measured with Langmuir probes, which are installed at the divertor plates near midplane of 7 toroidal sections out of the total of 10 sections, as shown in Fig.1 (a) [29,30]. Each toroidal section has two divertor arrays, which are named "Left (L)" and "Right (R)," as indicated in Fig.1 (a). The two arrays, L and R, connect to the Left and Right divertor legs shown in Fig.1 (b). At each plate, 20 probe pins of 2 mm diameter are placed with 6 mm intervals to cut the strike lines of the divertor legs. In this paper, the particle flux is analysed as a measure of the toroidal distribution of detachment.

Figure 6 shows time traces of the ion saturation current summed up over 20 pins at each toroidal section, #2, #4, #6, #7, #8, and #10, with (red lines) and without (black lines) RMP, with the letters "L" and "R" indicating the two arrays. As seen in the figure, the absolute values of the flux are different between the plates. These differences are caused by the slight difference in the divertor plate alignment and in the erosion/deposition processes of the probe pins at different toroidal sections. Therefore, in the present analysis comparison of the absolute values between the divertor plates is avoided. Instead, temporal change or change caused by RMP application with respect to the reference distribution without RMP are discussed.

Without RMP, the divertor particle flux increases with increasing density, although the trend is not exactly same

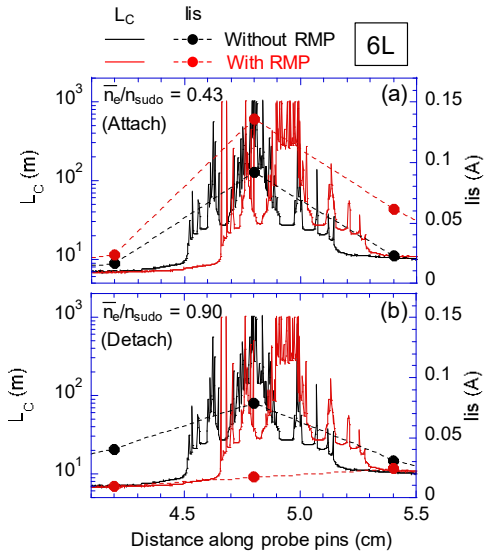

Fig.8 L_C (solid lines) and divertor particle flux (Iis, dashed lines with circles) profiles along the divertor probe pins at 6L divertor plate, with (red) and without (black) RMP. (a) $\bar{n}_e/n_{Sudo}$ = 0.43 (attached with RMP), (b) $\bar{n}_e/n_{Sudo}$ = 0.90 (detached with RMP).

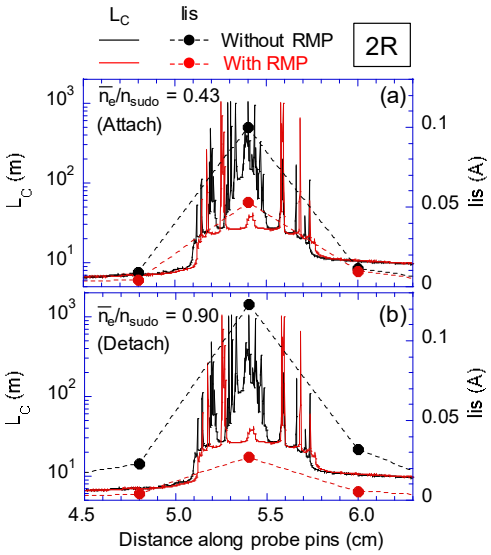

Fig.9 L_C (solid lines) and divertor particle flux (Iis, dashed lines with circles) profiles along the divertor probe pins at 2R divertor plate, with (red) and without (black) RMP. (a) $\bar{n}_e/n_{Sudo}$ = 0.43 (attached with RMP), (b) $\bar{n}_e/n_{Sudo}$ = 0.90 (detached with RMP).

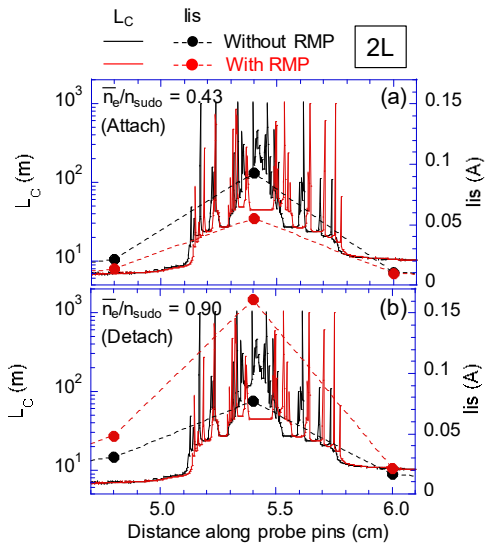

Fig.10 L_C (solid lines) and divertor particle flux (Iis, dashed lines with circles) profiles along the divertor probe pins at 2L divertor plate, with (red) and without (black) RMP. (a) $\bar{n}_e/n_{Sudo}$ = 0.43 (attached with RMP), (b) $\bar{n}_e/n_{Sudo}$ = 0.90 (detached with RMP).

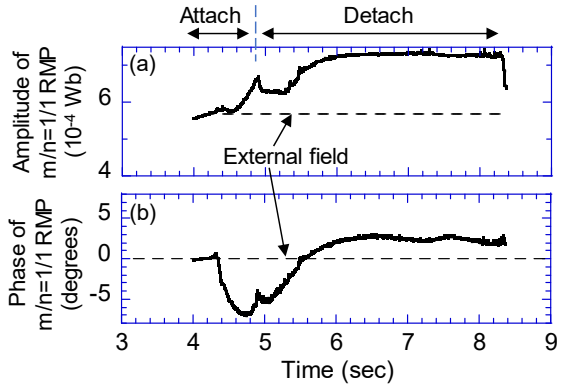

Fig.11 (a) Amplitude and (b) phase of the m/n/=1/1 RMP field including both external and plasma response. The amplitude and the phase of the external RMP field are indicated by dashed lines. The same shot as in Fig.1 with RMP (#128188).

between the different plates. The particle flux starts to decrease only just before the radiation collapse at t = 5.9 sec. Some of the section, for example, 2L, 6L etc., show decrease in the flux at earlier phase. Such difference between the divertor plates, which is ideally not expected, may come from toroidal asymmetry caused by toroidal localization of gas puffing and the NBI, etc.

Table 1 List of densities (timings) for profile analysis in Figs. 7, 8, 9, 10, 12, and 14.

$\bar{n}_e/n_{sudo}$	Without RMP (#128195)			With RMP (#128188)		
	$\bar{n}_e$ (10^{19} m^{-3})	a_{99} (m)	Time (sec)	$\bar{n}_e$ (10^{19} m^{-3})	a_{99} (m)	Time (sec)
0.43	3.8	0.59	4.433	3.8	0.56	4.633
0.90	8.6	0.57	5.566	8.7	0.48	5.666
1.0	9.7	0.51	5.800	9.8	0.48	6.033

With RMP application, the particle flux decreases at most of the divertor plates after detachment transition, t = 4.9 sec, except for those at 2L, 8L, where the flux even increases after the detachment transition. The timings of the flux reduction are also different at the different toroidal position, e.g., the flux at 2R, 10L starts to decrease far in advance of the detachment transition (t = 4.9 sec), while those at 4L, 6L etc., continue to decrease slowly even after the detachment transition.

In what follows, the toroidal variation of the divertor particle flux caused by RMP is analysed by taking the distribution without RMP as a reference. For the profile analysis in Figs. 7, 8, 9, 10, 12, and 14, the specific densities, normalized by n_{Sudo}, are selected from the two discharges, #128188 and #128195, as listed in Table 1 together with the line averaged density, a_{99}, and timings, with and without RMP.

Shown in Fig.7 are toroidal distributions of the divertor particle flux with RMP normalized by those without RMP at $\bar{n}_e/n_{Sudo}$ = 0.43 (attached phase with RMP) and 0.90 (detached phase with RMP), respectively. Here we excluded the section, where the probe pins around the strike lines cause malfunction. It is seen that the toroidal distribution is largely modulated by RMP application with respect to the reference distribution without RMP. At $\bar{n}_e/n_{Sudo}$ = 0.43 (the attached phase with RMP), the flux increases at 4L, 6L, 7L, 8R, and 9R, and decreases at other plates with respect to the reference case. The global change in toroidal direction indicates n = 1 mode structure but with phase shift between L and R divertor plates. In the detached phase, the particle flux at most of the divertor plates decreases with respect to the no RMP case, as shown in Fig.7 (b), except for 2L, 9R, where substantial increase is observed by a factor of 1.8 at maximum. The global profile still indicates n = 1 mode structure but with a different toroidal phase from the attached phase.

In the attached phase, the modulation of the flux is generally correlated to the increase of L_C at the footprint caused by RMP application as follows. As an example, L_C profiles along the probe pins at 6L are plotted in Fig.8 (a) with and without RMP, together with the particle flux profiles measured by the probes at $\bar{n}_e/n_{Sudo}$ = 0.43 (attached phase). The L_C's are calculated up to 1 km with a vacuum magnetic field application. A bundle of flux tubes are connected to the divertor plate with 6.5 mm width, which is comparable to the probe pin interval, so that we can not discuss the effects of the detailed profiles of L_C within the bundle. Nevertheless, we still see the effects qualitatively on the particle flux profile measured by the probe. By applying RMP, the footprint shifts toward the right side with increased L_C. The measured particle flux increases in the absolute values due to the longer L_C, as seen also in Fig.7 (a). The flux profile becomes more asymmetric with respect to the central peak, being increased

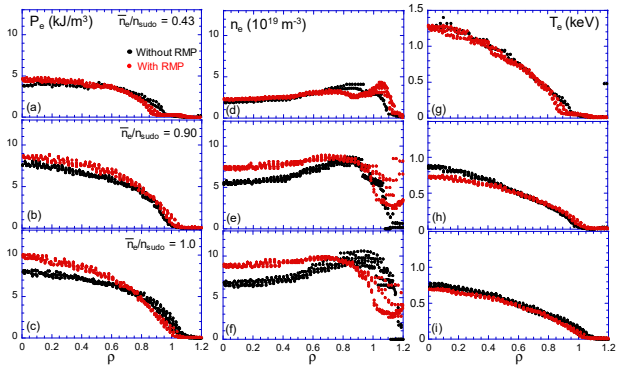

Fig. 12 Radial profiles of (a-c) electron pressure, (d-f) electron density, and (g-i) electron temperature at the different densities, $\bar{n}_e/n_{Sudo}$ = 0.43 (a,d,g), 0.90 (b, e, h), and 1.0 (c, f, i). Red: with RMP, black: without RMP. The radius of plasma volume, r_{eff}, is normalized with a_{99} at each timing, i.e. $\rho = r_{eff}/a_{99}$.

at the right side, which reflects the right shift of the footprint. On the other hand, the 2R plate shows decrease of the particle flux with RMP application, as seen in Fig.7 (a). This is considered due to the decreases in L_C, as shown in Fig.9 (a), where the long L_C bundle at the central region almost disappears completely with RMP, and thus the particle flux decreases as well. The results show that the particle transport is well correlated with the L_C distribution, to a certain extent, obtained by the vacuum approximation, and thus can be controlled by the RMP application in the attached phase.

At the detached phase, $\bar{n}_e/n_{Sudo}$ = 0.90, the particle flux both at 6L and 2R decreases in the entire region with respect to the case without RMP, as shown in Fig.8 (b) and Fig.9(b).

The behavior of particle flux at 2L plate is not straightfoward. At this plate, the flux becomes smaller by applying RMP in the attached phase with respect to the reference case, but particle flux increases at the detached phase, as shown in Fig.7. The profiles of L_C and particle flux at 2L plate are shown in Fig.10 for the attached and detached phases. In this plate, the longer flux tubes, e.g., L_C > 100 m, decreases, but the area of L_C ~ 30 m increases with RMP. The reduction of the flux at the attached phase may be due to the reduction of L_C > 100 m. On the other hand, at the detached phase, the increases of the flux could be because the particle flux transport channel changes from long L_C > 100 m at the attached phase to the medium L_C ~ 30 m. This effect still must be explored by detailed analysis of the relation between magnetic field structure and the ionization front.

In LHD, significant plasma response to the external RMP field has been observed [31, 32], which is measured by the saddle loop coils [33, 34]. Shown in Fig. 11 are the amplitude of m/n = 1/1 RMP, which includes both the external and the plasma response field, and the phase of the m/n/ = 1/1 RMP relative to the external field, respectively. The actual plasma response has broad spectrum over different mode numbers. Here we extracted one which has m/n = 1/1 mode. It is found that the RMP is gradually amplified at the attached phase, while the phase is shifted in negative direction (clockwise in a top view of torus). After the detachment transition at t = 4.9 sec, the RMP is amplified further by up to ~ 30 %, and the phase is shifted to the positive direction (counter-clockwise in a top view of torus). These change of the magnetic field could modify the L_C distribution being different from those of vacuum approximation. Inclusion of the plasma response into the L_C calculation is a future work.

Mitigation scheme of the excessive flux at the plates with increased flux in the detached phase are under investigation by toroidal phase shift of RMP and additional local impurity seeding. The divertor power load estimation by analysing the probe characteristics of 280 pins in total is also an important but challenging task to assess the feasibility of the divertor plates.

3. Core plasma confinement during detachment with RMP

3.1 Global parameters

Temporal evolutions of electron pressure profiles are plotted in Fig.12, together with electron temperature (T_e) and

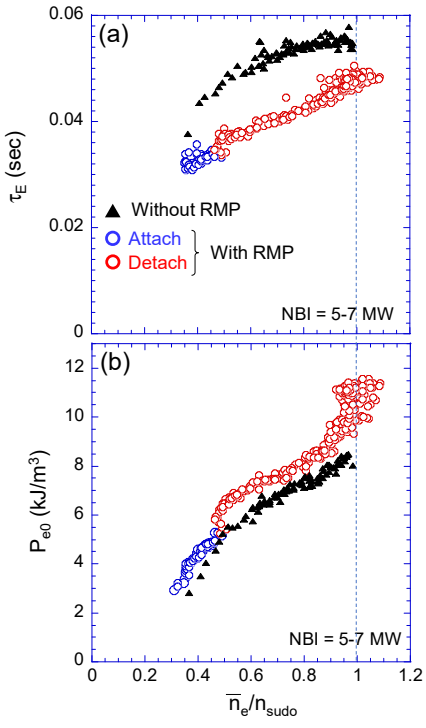

Fig.13 The density dependence of (a) the energy confinement time, τ_E, and (b) the central electron pressure, P_{e0}. Black triangles: without RMP. Blue circles: attached with RMP. Red circles: detached with RMP. The data points with NBI heating power of 5 to 7 MW are plotted.

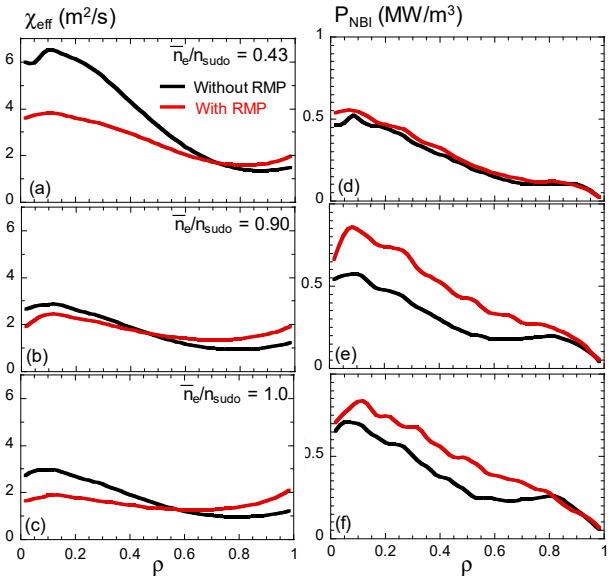

Fig.14 Radial profiles of (a,b,c) $\chi_{eff} = 0.5(\chi_e + \chi_i)$, and (d,e,f) NBI heating deposition, P_{NBI}, obtained by TASK-3D. $\bar{n}_e/n_{Sudo}$ = 0.43 (a,d), 0.90 (b, e), and 1.0 (c, f). Red: with RMP. Black: without RMP.

density (n_e) profiles with and without RMP application. The profiles are mapped to the normalized minor radius, $\rho = r_{eff}/a_{99}$, assuming symmetry profiles with respect to the center of plasma, $\rho = 0$. a_{99} is evaluated at each timing as shown in Fig.2 (g). Because of the normalization with a_{99}, the shrinkage of the plasma volume with the magnetic island with RMP application is not observable in these figures. At the low density, $\bar{n}_e/n_{Sudo}$ = 0.43, the pressure, n_e, and T_e profiles are almost identical for the cases with and without RMP. The flattening of T_e due to the edge magnetic island with RMP is visible at $\rho \sim 0.9$, which is, however, invisible at higher density due to the lowering of the flatening T_e, 10~20 eV, in the scale of Fig.12.With increasing density, the pressure and n_e gradually increase while T_e decreases. It is noted that the pressure becomes more peaked with RMP application at the high density range, where the plasma already detached at $\bar{n}_e/n_{Sudo} > 0.45$. It is seen that the enhanced peaking with RMP is caused by the difference in n_e at the central region, while T_e is almost same for the both cases. The clear change in the pressure gradient inside $\rho = 0.7$ is apparent at the highest density, $\bar{n}_e/n_{Sudo}$ = 1.0.

Density dependence of the energy confinement time, τ_E, and the central pressure, P_{e0}, are plotted in Fig.13. τ_E is systematically smaller in the case with RMP application because of the reduced volume due to the edge magnetic island as seen in a_{99} in Fig.2 (g). In the both cases, τ_E increases with increasing density. Without RMP τ_E saturates around $\bar{n}_e/n_{Sudo}$ = 0.8, which corresponds to the density where CV and CVI start to increase as shown in Fig.5. With RMP

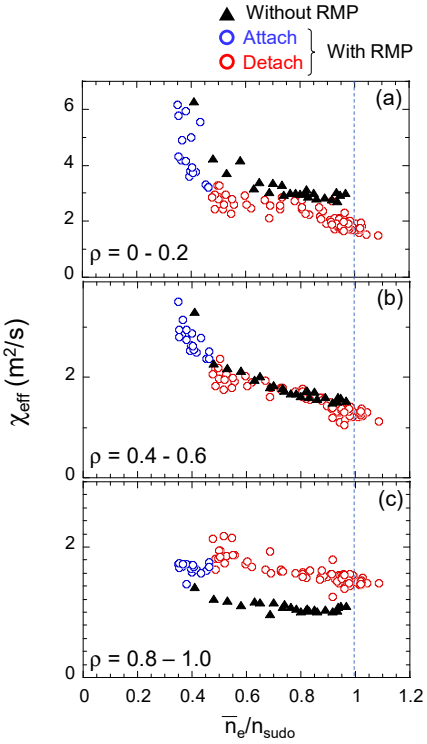

Fig.15 Density dependence of χ_{eff} averaged over $\rho = 0 - 0.2$ (a), $0.4 - 0.6$(b), $0.8 - 1.0$(c). Black triangles: without RMP. Blue circles: attached with RMP. Red circles: detached with RMP.

application, on the other hand, there exists discontinuity in the density dependence of τ_E as well as of P_{e0} at the detachment transition, $\bar{n}_e/n_{Sudo} \sim 0.45$. After the transition, τ_E continues to increase up to the density limit without saturation even with higher CV and CVI than the case without RMP (Fig.5). The enhancement in the central pressure, P_{e0} with RMP clearly appears after the detachment transition as seen in Fig.13 (b), and especially around the density limit the pressure peaking becomes significant. If we estimate a fusion triple product, $n_0\tau_E T_0$, from the τ_E and P_{e0}, it is comparable for the cases with and without RMP near the density limit.

The confinement enhancement factor, $\tau_E^{exp}/\tau_E^{ISS04}$, where τ_E^{ISS04} is the sterallator energy confinement scaling [35], was evaluated in ref.[19], taking into account the change of plasma radius a_{99}. It is found that the enhancement factor becomes larger with RMP during the detached phase.

3.2 Core transport analysis

The global parameters are largely affected by the change of the plasma volume caused by the edge magnetic island. In order to address the local plasma transport characteristics, a core transport analysis has been performed with TASK3D, which is a 1D radial transport code. The code calculates the heating source profile (in the present case, NBI) taking into account beam slowing down time and solves a heat conduction

equation with n_e and T_e profiles as an input from experiments [36].

The obtained NBI power deposition profiles and heat conductivity, $\chi_{eff} = 0.5(\chi_e + \chi_i)$, are plotted in Fig.14, where χ_e and χ_i are electron and ion heat conductivity. At the attached phase, $\bar{n}_e/n_{Sudo}$ = 0.43, the NBI power deposition profiles are almost identical for the cases with and without RMP, while χ_{eff} is smaller with the RMP at the central region. The large χ_{eff} at the central region without RMP is attributed to the very flat pressure profile at the central region, as seen in Fig. 12 (a). After the detachment transtion, i.e., $\bar{n}_e/n_{Sudo}$ = 0.90 and 1.0, the power deposition becomes more peaked with RMP, which is due to the deeper penetration of the beam because of the shrinkage of the plasma volume with the edge radiation. The increased energy deposition at the central region with RMP, ~ 0.3 MW/m^3, provides particle source increment, Sp, of order of 10^{19} 1/s/m^3, as estimated from the NBI energy of 180 keV. If we assume simple diffusive particle transport model, the Sp should give the increment of density, $\Delta n \sim S_p \Delta r^2 \frac{1}{D_\perp} = 10^{17} \sim 10^{18}\ m^{-3}$, with $\Delta r \approx 0.1 \sim 0.4\ m$ ($\Delta\rho \approx 0.2 \sim 0.8$), $D_\perp = 1\ m^2/s$. This is not sufficient to account for the density increase at the central region with RMP, ~ 10^{19} m^{-3}, as observed in Fig.12 (e,f). At the inner region, $\rho < 0.6$, χ_{eff} decreases significantly both with and without RMP at the higher density range, where χ_{eff} remains slightly smaller with the RMP, indicating that the pressure peaking may be due to the transport effect. At the periphery, $\rho > 0.8$, on the other hand, χ_{eff} becomes larger with RMP. This could be due to the stochastization of the magnetic field structure caused by RMP, which enhances radial transport with the braiding magnetic field lines [37,38]. The enhancement of impurity emission with RMP as shown in Figs.4 and 5 could also lead to larger χ_{eff} through the volumetric power loss at the edge, which is not taken into account in TASK-3D. At $\bar{n}_e/n_{Sudo}$ = 1.0, the NBI deposition also starts to be peaked in the case without RMP. This is due to the shrinkage of the plasma at the collapsing phase, while χ_{eff} remains almost the same profiles as that of $\bar{n}_e/n_{Sudo}$ = 0.90.

The density dependence of χ_{eff} averaged over $\rho = 0 - 0.2, 0.4 - 0.6, 0.8 - 1.0$, respectively, are plotted in Fig.15. The decrease in χ_{eff} toward higher density range is more pronounced at the inner region, $\rho = 0 - 0.2$. Near the density limit, χ_{eff} saturates at the central region without RMP, while those with RMP continues to decrease up to the density limit. The behaviour is qualitatively consistent with the density dependence of τ_E, as shown in Fig.13. On the other hand, χ_{eff} 's at ρ = 0.4-0.6 and 0.8-1.0 show similar density dependence for the both cases, but with larger χ_{eff} at the periphery with RMP. The results suggest that the qualitative difference in the density dependence of τ_E between the cases with and without RMP is attributed to the transport at the central region. If the enhanced transport at the periphery, ρ = 0.8 – 1.0, with RMP is due to the stochastization, it may be effective for impurity screening or exhaust of He as discussed in ref.[25,26].

At the moment, we would like to avoid precise argument about quantitative magnitude of χ_{eff} since the accuracy of χ_{eff} by TASK-3D is under assessment, and thus we need further statistical analysis by accumulating discharges. Nevertheless, these results show that, at least, there is no significant transport degradation at the central region during detached phase with RMP application compared to the case without RMP, even with the enhanced impurity radiation and reduced divertor particle flux. From the impurity emission measurements, the carbon impurity content inside LCFS could be larger with RMP application as discussed in section 2.3. Although the coupling between impurity content and the core transport is beyond the scope of this paper, it is here worthwhile to note that there is experimental evidence of the correlation between transport improvement and impurity [39,40,41,42]. Further analysis on this issue is left for future work.

4. Summary

The effects of RMP application on the detachment operation in LHD have been investigated in terms of impurity radiation, toroidal distribution of detachment, and the core plasma transport. By applying the RMP, which creates edge remnant magnetic island in the stochastic layer, the detachment transition is induced at the lower density with enhanced radiation.

The discharge can be sustained stably around the density limit with detached divertor operation with RMP. Clear change in the density dependence of the radiated power by RMP aplication occurs by enhanced impurity emission of lower charge states, C^{2+} and C^{3+}, which radiate around the island. The weakened sensitivity of the radiated power against the density by RMP aplication leads to easier control of the discharge with enhanced radiation. The mechanism of the qualitative change of the radiation with RMP is under investigation.

The divertor particle flux is significantly modulated in toroidal direction by RMP application with n = 1 mode structure, which is closely correlated with the change of L_C footprint, in vacuum approximation, caused by RMP, especially in the attached phase. In the detached phase, the particle flux is reduced almost entirely in toroidal direction except for a few sections, where the flux increases by up to a factor of 2 with respect to the no RMP case. The pattern exhibits n = 1 mode structure but in a phase shifted with respect to the attached case. Either or both change of transport channel flux tubes or/and plasma response to the equilibrium

magnetic field could be responsible for the observations. Mitigation of the excessive particle flux is under investigation.

The energy confinement time is systematically shorter in the case with RMP than without RMP, due to the reduced plasma volume caused by the edge magnetic island and by the radiation therein. However, the pressure peaking is observed during the detached phase with RMP, which can provide higher fusion triple product than without RMP near the density limit, compensating the reduction of energy confinement time. The core transport analysis, taking into account the NBI power deposition profiles, shows that there is no significant transport degradation with RMP application in the central region, with the enhanced radiated power loss and the divertor detachment.

These results suggest possible means to operate with divertor detachment compatible with a good core confinement by using 3D edge magnetic field structure as a control knob.

Acknowledgements

One of the authors, M.K., is grateful for the fruitful discussions with Prof. R. Sakamoto, Prof. K.Y. Watanabe, Prof. B.J. Peterson, and Prof. M.Z. Tokar. The work has been financially supported by JSPS KAKENHI Grant Number JP16H04622, 19H01878 and NIFS budget code ULPP026.

References

[1] Huber, A. et al., 2013 J. Nucl. Mater. **438** S139.
[2] Asakura, N. et al., 2009 Nucl. Fusion **49** 115010.
[3] Evans, T.E. et al., 2008 Nucl. Fusion **48** 024002.
[4] Suttrop W. et al 2011 Phys. Rev. Lett. **106** 225004.
[5] Jeon Y.M. et al 2012 Phys. Rev. Lett. **109** 035004
[6] Ghendrih Ph. et al 2002 Nucl. Fusion **42** 1221
[7] Finken K.H. et al 1999 Nucl. Fusion **39** 637
[8] Loarte, A., et al. 2014 Nuclear Fusion **54** 033007.
[9] Evans, T.E. et al., 2013 Nucl. Fusion **53** 093029.
[10] Schmitz, O. et al., 2016 Nucl. Fusion **56** 066008.
[11] Kim K. et al. 2017 Physics of Plasmas **24** 052506.
[12] Brida D. et al., 2017 Nucl. Fusion **57** 116006.
[13] Faitsch M. et al., 2017 Nuclear Materials and Energy **12** 1020.
[14] Ahn J.W. et al., 2017 Plasma Phys. Control. Fusion **59** 084002.
[15] Kobayashi M. et al., 2013 Nucl. Fusion **53** 093032.
[16] Pandya S.N. et al., 2016 Nuclear Fusion **56** 046002.
[17] Zhang H.M. et al., 2017 Physics of Plasmas **24** 022510.
[18] Kobayashi M. et al., 2010 Phys. Plasmas **17** 056111.
[19] Kobayashi M. et al., 2018 Nuclear Materials and Energy **17** 137.
[20] Ohyabu N. et al 1994 Nucl. Fusion **34** 387
[21] Takeiri Y. et al., 2017 Nucl. Fusion **57** 102023.
[22] Sudo, S. et al., 1990 Nucl. Fusion **30** 11.
[23] Susuki, C. et al., Plasma Phys. Control. Fusion **55** (2013) 014016.
[24] Zhang H.M. et al., 2016 Plasma and Fusion Research **11** 2402019.
[25] Chowdhuri M.B. et al., 2009 Physics of Plasmas **16** 062502.
[26] Schmitz O. et al., 2016 Nucl. Fusion **56** 106011.
[27] Feng Y. et al., 2006 Nucl. Fusion **46** 807.
[28] Pedersen T.S. et al., this conference, "FIRST DIVERTOR PHYSICS STUDIES IN WENDELSTEIN 7-X", submitted to Nuclear Fusion.
[29] Tanaka H. et al., 2017 Nuclear Materials and Energy **12** 241.
[30] Masuzaki S. et al., 2019 Nuclear Materials and Energy **18** 281.
[31] Ohyabu N. et al., Plasma Phys. Control. Fusion **47** (2005) 1431.
[32] Narushima Y. et al., 2013 Plasma and Fusion Research **8** 1402058.
[33] Narushima Y. et al., Plasma and Fusion Research, 2 (2007) S1094.
[34] Narushima Y. et al., 2017 Nucl. Fusion **57** 076024.
[35] Yamada, H. et al., Nucl. Fusion **45** (2005) 1684.
[36] Yokoyama M. et al., 2017 Nuclear Fusion **57** 126016.
[37] Rechester A.B. and Rosenbluth M.N. 1978 Phys. Rev. Lett. **40** 38.
[38] Tokar M.Z. 1999 Phys. Plasmas **6** 2808.
[39] Ongena J. et al., 1996 Plasma Phys. Control. Fusion **38** 279.
[40] Tokar M.Z. et al., 2000 Phys. Rev. Lett. **84** 895.
[41] Osakabe M. et al., 2014 Plasma Phys. Control. Fusion **56** 095011.
[42] Mukai K. et al., 2018 Plasma Phys. Control. Fusion **60** 074005.